Supporting Information for

Enhanced Broad-Frequency Electromagnetic-Wave Absorption and Environmental Stability of Carbonitriding High-Entropy Alloys via a Green Mechanochemical Approach

Jiawen Hu[a], Linwen Jiang[a, *], Jiawei Jin[a], Hang Liu[a], Anhua Wu[b], Xiaofeng Zhang[c, *]

[a]School of Materials Science and Chemical Engineering, State Key Laboratory Base of Novel Functional Materials and Preparation Science, Ningbo University, Ningbo 315211, PR China

[b]Shanghai Institute of Ceramics, Chinese Academy of Sciences, Shanghai 201800, PR China

[c]Institute of New Materials, Guangdong Academy of Science, National Engineering Laboratory for Modern Materials Surface Engineering Technology, Guangzhou 510651, PR China

[*] Corresponding author.

Corresponding author.

E-mail addresses: jianglinwen@nbu.edu.cn (Linwen Jiang), zhangxiaofeng@gdinm.com (Xiaofeng Zhang).

The details of corrosion resistance test are as follows:

(1) An electrochemical workstation (CHI760E) is used to test the potentiodynamic polarization curve and electrochemical impedance spectra (EIS) in the 3.5 wt.% NaCl solution. The electrochemical tests adopt a three-electrode system. A sample-loaded carbon paper is used for the working electrode, and a platinum metal sheet and saturated calomel electrode (SCE) are used as auxiliary and reference electrodes, respectively. The open-circuit potential of samples is obtained after being soaked for 1800 s. The potentiodynamic polarization curves are measured at a scanning rate of 0.5 mV/s. Corrosion potential and corrosion current density are obtained from polarization curves. The EIS test is carried out with a scan amplitude of 5 mV and a frequency range of 100 kHz - 0.1 Hz.

(2) The samples were prepared as follows: first, 5 mg of sample powder, 120 μL of naphthol, 200 μL of isopropanol and 600 μL of deionized water were uniformly mixed. Subsequently, 35 μL of the mixed solution was added dropwise onto a carbon paper with size of 0.5 × 0.5 cm^2. Finally, these samples were dried at 60 °C for 10 minutes.

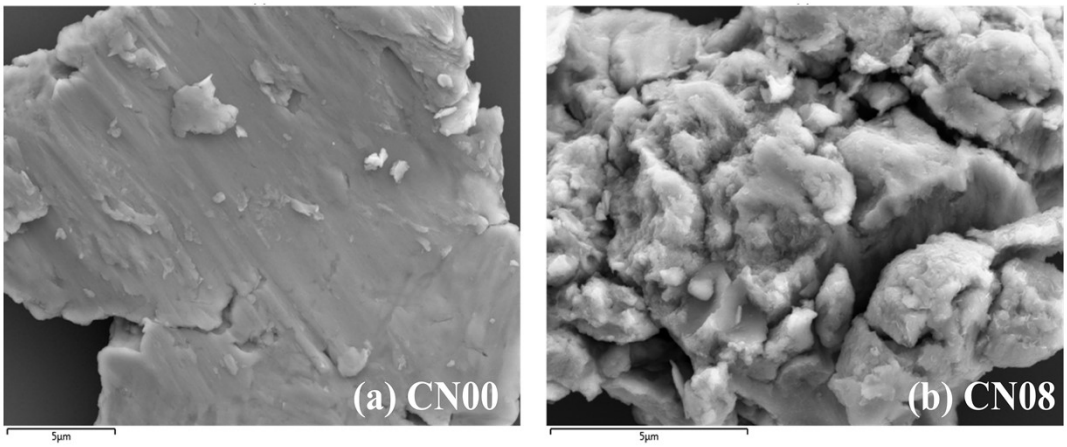

Fig. S1. Comparison of surface morphology between (a) CN00 and (b) CN08.

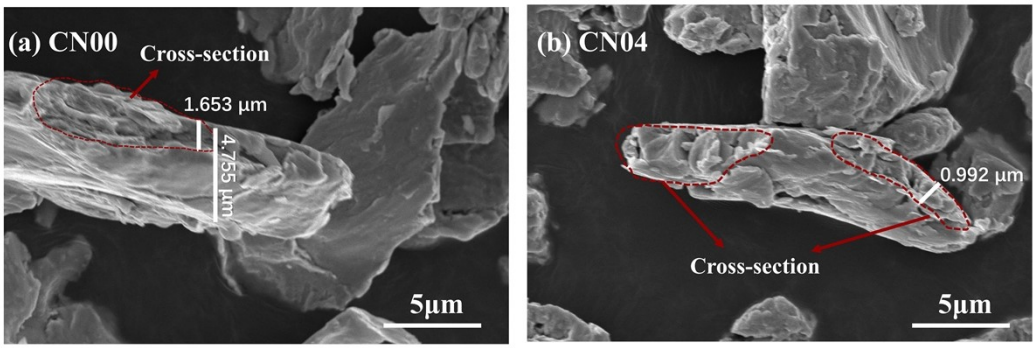

Fig. S2. Cross-section of (a) CN00 and (b) CN04.

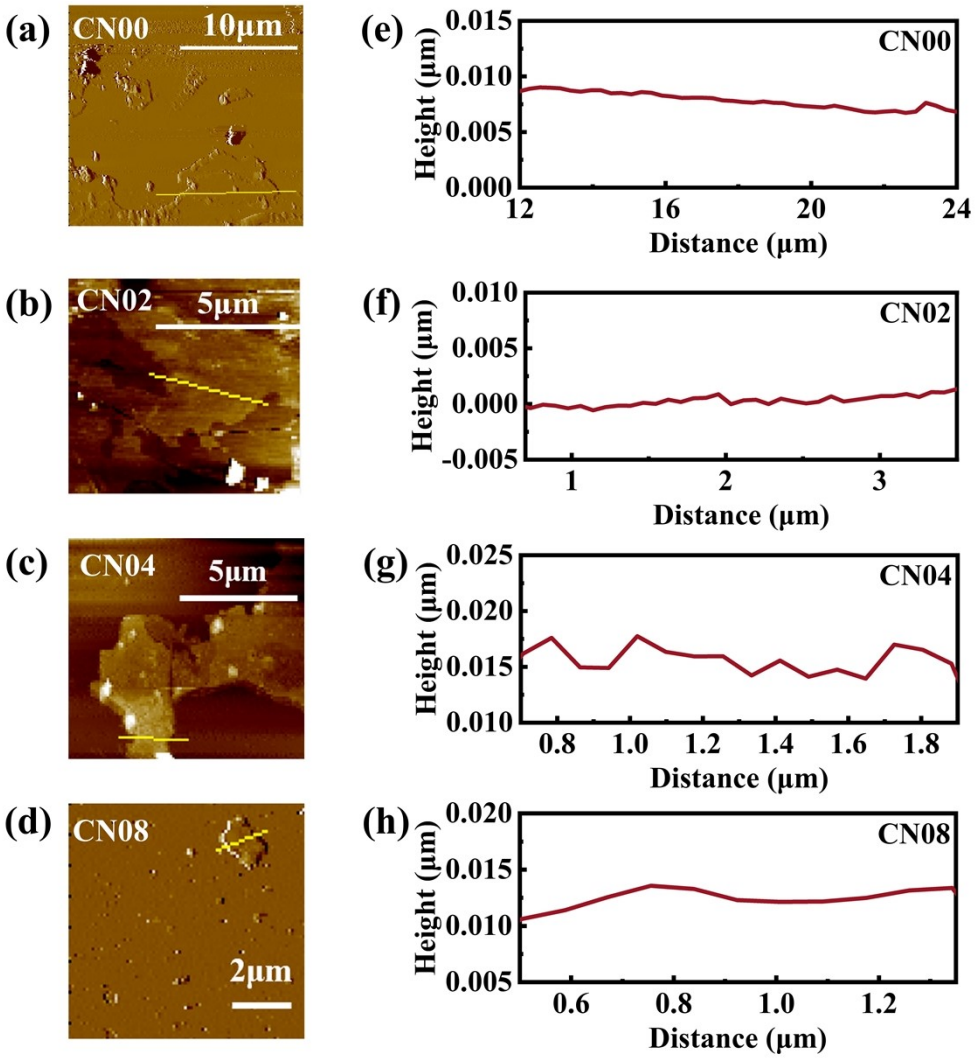

Fig. S3. (a−d) AFM images and (e-h) height profiles of CN00, CN02, CN04 and CN08.

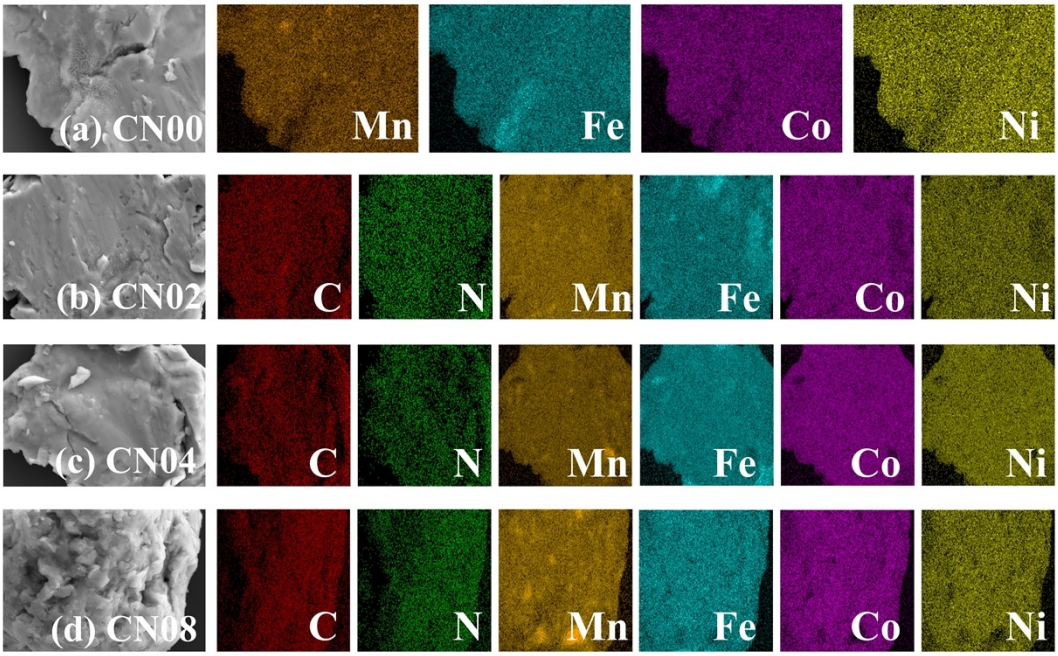

Fig. S4. EDS element mapping images of (a) CN00, (b) CN02, (c) CN04 and (d) CN08.

Table S1. Melting point, crystal structure, atomic radius and Pauling electronegativity of raw materials.

Element	Fe	Co	Ni	Mn	$C_3H_2N_2$
Melting point (°C)	1538	1495	1455	1246	30-32
Crystal structure	BCC	HCP	FCC	BCC	-
Atomic radius (pm)	126	125	124	127	-
Pauling electronegativity	1.83	1.88	1.91	1.55	-

Table S2. Chemical compositions (atom percent) for sample CN00, CN02, CN04 and CN08.

Samples	Fe	Co	Ni	Cu	C	N
CN00	28.01	24.14	25.04	22.81	/	/
CN02	21.56	18.07	18.63	18.58	21.49	1.66
CN04	21.76	18.13	18.78	19.13	20.42	1.78
CN08	18.71	18.03	18.34	17.72	23.97	3.23

The results of Table S2 showed that different principal metal elements in CN00, CN02, CN04, and CN08 were evenly distributed. However, the C and N contents obtained by EDS were not accurate, especially for C, which may be due to: (1) The carbon conductive adhesive used in the test resulted in excessive C content. (2) There may be carbon pollution in the electron microscope vacuum system. When the electron beam hits the sample, the surrounding carbon rapidly migrates to the area scanned by the electron beam, causing the sample with a high carbon content. (3) EDS can only carry out qualitative and semi-quantitative element analysis, and the measurement results of light elements such as C, N, and O are not accurate.

The particle size of each sample was analyzed using the LPSA test, and the results are shown in Fig. S5. The average particle size of the samples gradually decreased from 20.16 μm (CN00) to 2.39 μm (CN08), which is consistent with the results of the particle size distribution graph in Fig. 3.

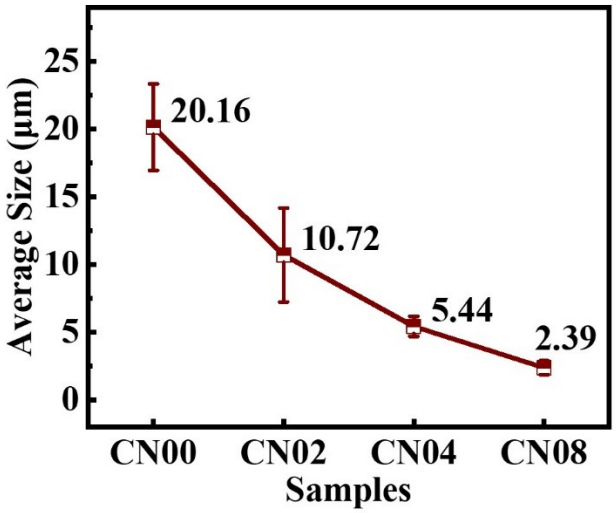

Fig. S5. The average size measured by LPSA of all samples (CN00, CN02, CN04 and CN08).

Meanwhile, the degree of lattice distortion was analyzed, which can be reflected by the strain within the carbonitriding FeCoNiMn HEAs. When small-sized C and N atoms were introduced into the HEAs, it would lead to lattice distortion. The presence of C and N in the lattice interstitials cause the increase of the lattice parameters, which in turn enhanced the strain in the HEAs. Therefore, as shown in Fig. S6, the strain increased from 0.877 (CN00) to 1.544 (CN08) with the increase of C and N contents in the HEAs.

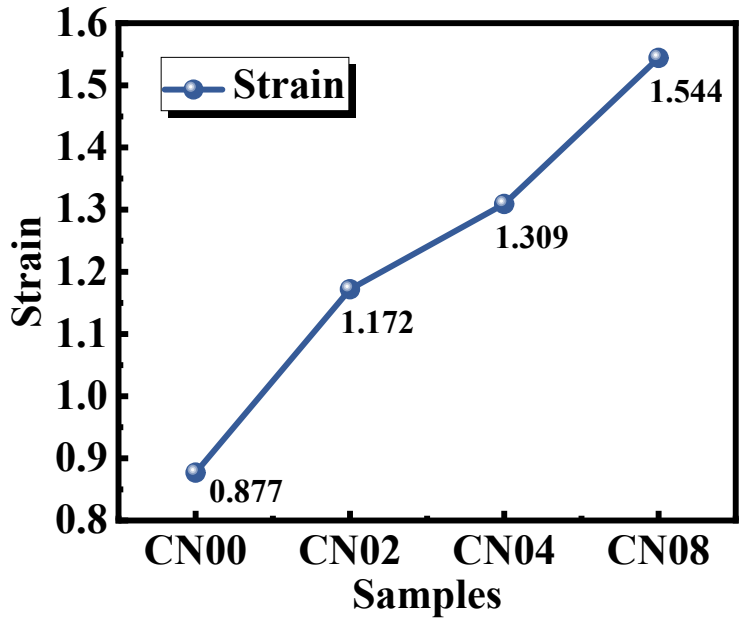

Fig. S6. The strain of all carbonitriding FeCoNiMn HEAs samples.

Table S3. Comparison of corrosion-resistance performances of different HEAs.[1-6]

Samples	Solution	I_{corr} ($\mu A/cm^2$)	E_{corr} (mV)	Ref.
FeCoNiCu	3.5 wt.% NaCl	5.78	-0.43	Ref. 1
$FeCoNiCuAlCe_{0.01}$	3.5 wt.% NaCl	5.27	-0.43	Ref. 1
$FeCoNiCuAlCe_{0.03}$	3.5 wt.% NaCl	4.61	-0.43	Ref. 1
$FeCoNiCuAlCe_{0.09}$	3.5 wt.% NaCl	4.01	-0.45	Ref. 1
$FeCoNiAl_{0.3}$	3.5 wt.% NaCl	5.02	-0.204	Ref. 2
FeCoNiCrBSiNb	3.5 wt.% NaCl	5.20	-0.390	Ref. 3
$Ti_{21.6}Al_{11.3}Cr_{19.4}Si_{23.5}V_{22.0}O_{2.2}$	3.5 wt.% NaCl	6.14	-0.541	Ref. 4
FeCoNiCr	3.5 wt.% NaCl	2.51	-0.036	Ref. 5
FeCoNiMn	3.5 wt.% NaCl	4.9	-163	Ref. 6
CN08	3.5 wt.% NaCl	3.05	-39.33	This work

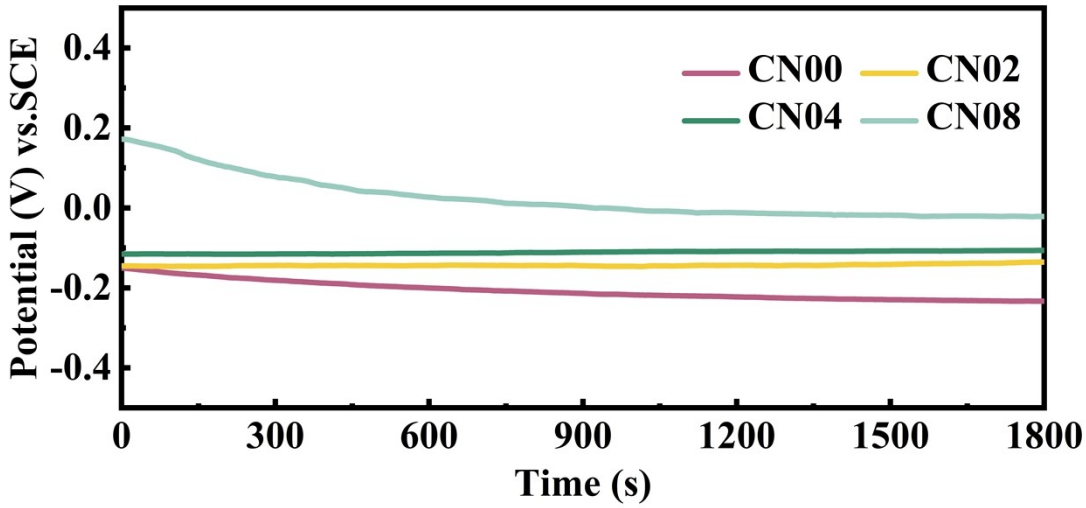

Fig. S7. Open-circuit potentials of carbonitriding FeCoNiMn HEAs.

Table S4. The comparison of mechanical properties of related similar materials. [7–11]

Samples	Nanohardness (GPa)	Young's modulus (GPa)	Ref.
FeCoNiCr HEAs	4.3	150	Ref.7
	7.0	202	Ref.7
	6.2	211	Ref.7
	2.9	180	Ref.7
	7.5	213	Ref.7
	7.3	215	Ref.7
	4.3	242	Ref.7
CoCrFeNiMn HEAs	2.7	222	Ref.8
	2.8	215	Ref.8
	2.89	224	Ref.8
	2.93	209.5	Ref.8
	2.98	228	Ref.8
	3.05	221	Ref.8
	4.7	245	Ref.8
	5.7	246	Ref.8
Stainless steel	4.5	0.32	Ref.9
	4.8	0.58	Ref.9
	3.43	177	Ref.10
	3.61	185.6	Ref.10
	3.64	196	Ref.10
	3.62	187.5	Ref.10
	3.38	174.8	Ref.10
	3.42	184	Ref.11
	4.44	187	Ref.11
CN04	4.92	38.58	This work

Specifically, the dielectric loss can be expressed with the Debye equation as follows:

$$\varepsilon_r = \varepsilon' - j\varepsilon'' = \varepsilon_\infty + \frac{\varepsilon_s - \varepsilon_\infty}{1 + j2\pi f\tau} \quad (1)$$

$$\varepsilon' = \varepsilon_\infty + \frac{\varepsilon_s - \varepsilon_\infty}{1 + (2\pi f)^2\tau^2} \quad (2)$$

$$\varepsilon'' = \varepsilon_P + \varepsilon_C = \frac{(\varepsilon_s - \varepsilon_\infty)2\pi f\tau}{1 + (2\pi f)^2\tau^2} + \frac{\sigma}{2\pi f\varepsilon_0} \quad (3)$$

where ε_s is the static dielectric constant and ε_∞ is the dielectric constant of infinite frequency and τ is the relaxation time, σ is the conductivity, and ε_p and ε_c is the polarization loss and the conductivity loss, respectively. The dielectric losses result from polarization losses caused by the establishment of polarization and conductivity losses caused by carrier transfer. To further investigate the mechanism of dielectric losses in materials, we did the following derivations. The equation S1 can be obtained if there are no conductivity losses, and equation S2 is derived from equation S3 using equation 2.

$$\varepsilon'' = \varepsilon_P + \frac{(\varepsilon_s - \varepsilon_\infty)2\pi f\tau}{1 + (2\pi f)^2\tau^2} \quad (S1)$$

$$\frac{\varepsilon''}{f} = 2\pi\tau\varepsilon' - 2\pi\tau\varepsilon_\infty \quad (S2)$$

$$\varepsilon'' = \varepsilon_C = \frac{\sigma}{2\pi\varepsilon_0} f^{-1} \quad (S3)$$

Because τ and ε_∞ are constants, plotting ε''/f and ε' will give a straight line when there is no conductivity loss. In other words, when the ε''/f-ε' plots is straight, there is no conductivity loss occurring. Secondly, equation 3 is converted into equation S3 assuming no polarization loss. Because σ is a constant, the ε''-f^{-1} plot will be a straight line when there is no polarization loss. In other words, when the ε''-f^{-1} plots is straight, there is no polarization loss occurring.

To further assess the polarization process of carbonitriding FeCoNiMn HEAs, the ε''-ε' curve is depicted using the aforementioned Debye equation, as presented in Fig. S8 (in supporting material). According to Debye's theory, each semicircle (referred to the Cole-Cole semicircle) is associated with a distinct polarization relaxation process. Cole-Cole semicircles can be observed in Fig. S8(a-d), suggesting that a notable polarization relaxation process takes place in the carbonitriding FeCoNiMn HEAs, which is beneficial for the absorption of electromagnetic waves. CN04 exhibits the most pronounced Cole-Cole semicircle, indicating a stronger Debye relaxation, which is also confirmed by the forms of the ε'' and $tan\delta_{\varepsilon}$ curves.

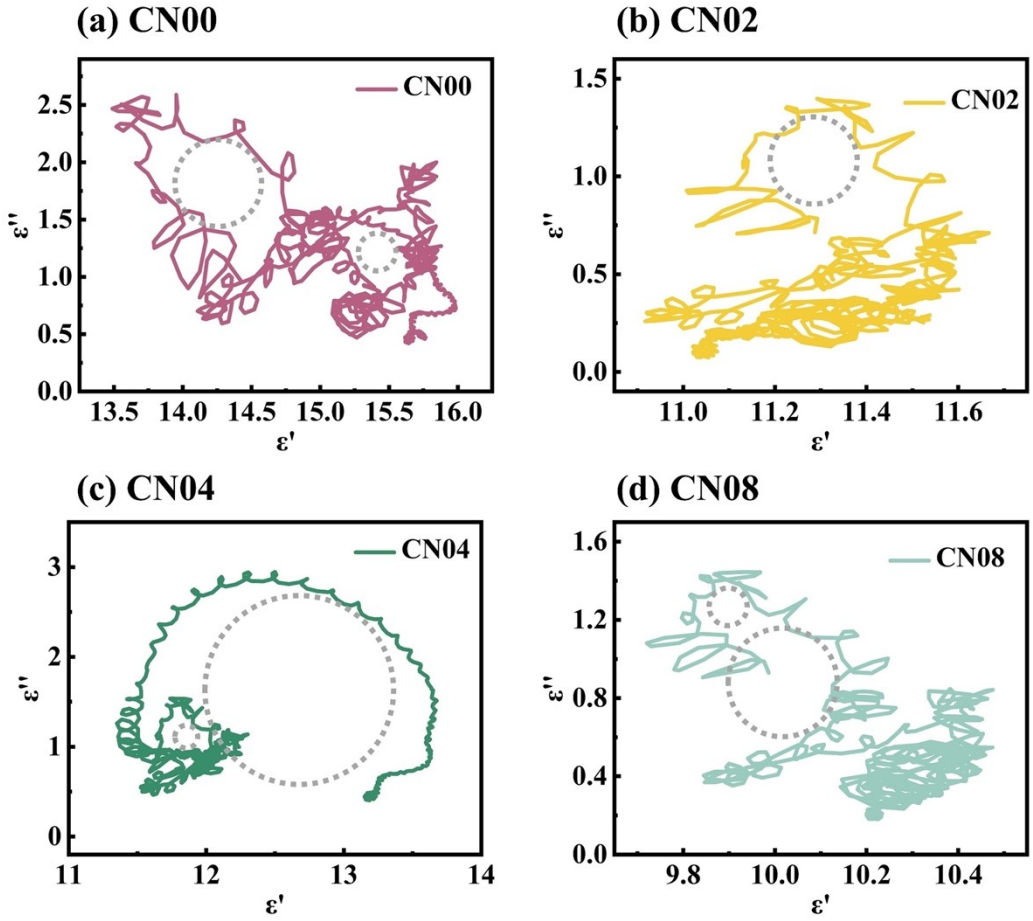

Fig. S8. The Cole–Cole semicircle patterns of (a) CN00, (b) CN02, (c) CN04 and (d) CN08.

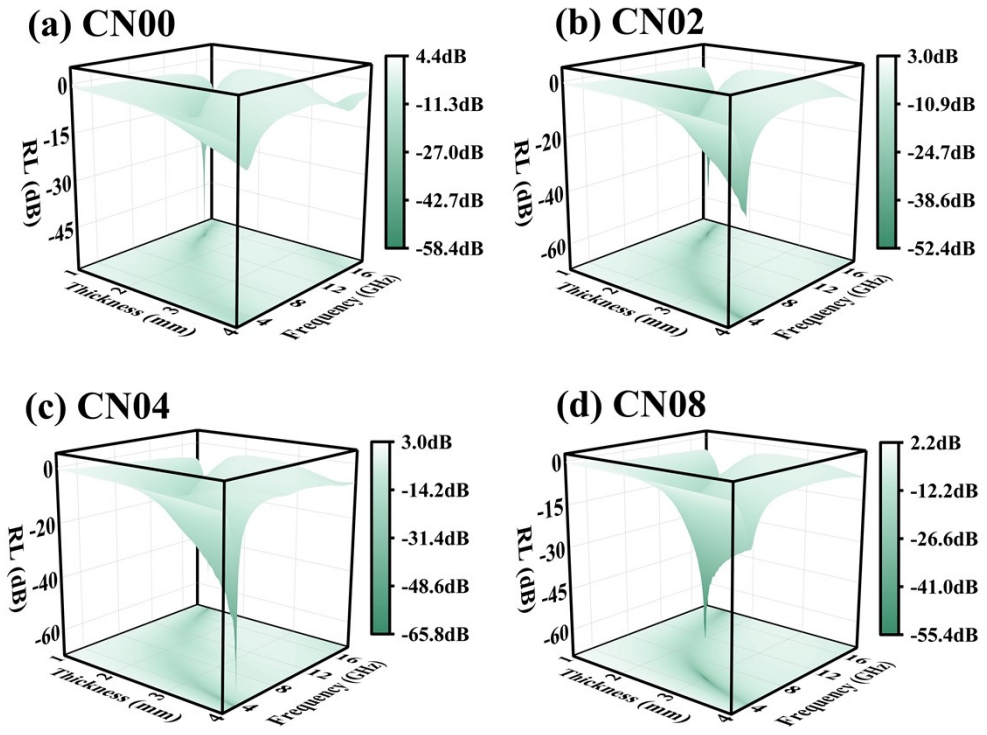

Fig. S9. The 3D RL plots as a function of frequency at various thicknesses of (a) CN00, (b) CN02, (c) CN04 and (d) CN08.

Table S5. The comparison of RL performances of all samples in this work.

Samples	RL_{min} (dB)	Frequency (GHz)	Thickness (mm)
CN00	-58.4	14.42	1.42
CN02	-52.4	15.36	1.52
CN04	-65.8	3.44	4.00
CN08	-55.4	5.48	3.00

Table S6. The comparison of comprehensive properties with related materials.[1, 5, 10, 12-17]

Samples	RL (dB)	F (GHz)	EAB (GHz)	Thickness (mm)	Nanohardness (GPa)	I_{corr} (μA/cm^2)	Ref.
CN04	-65.8	3.44	5.48	1.41	4.92	3.01	This work
CN08	-55.4	5.48	7.76	1.62	0.59	3.05	This work
$FeCoNiCuS_{0.2}$	-55.4	6.52	7	2.16	/	3.59	Ref.12
$FeCoNiCuC_{0.04}$	-61.1	15.28	5.1	1.6	3.4	5.14	Ref.13
$FeCoNiCuC_{0.10}$	-59.9	6.78	5.2	2.8	0.4	9.25	Ref.13
$FeCoNiCuC_{0.1}N_{0.2}$	-32.3	7.89	4.46	2.5	4.27	2.43	Ref.14
$FeCoNiCrB_{0.01}$	-64.5	12.43	5.08	2.66	4.5	8.729	Ref.5
HCN_S	-45.7	/	3.9	3.6	/	/	Ref.15
$FeCoNiMn_{0.5}Al_{0.2}$	-44.4	/	3.825	3	/	/	Ref.16
$FeCoNiCuAlCe_{0.09}$	/	/	/	/	/	4.01	Ref.1
$FeCoNiCuC_{0.09}N_{0.18}$	-55.8	15.82	3.82	2.38	1.75	0.51	Ref.17
Stainless steels					3.38		Ref.10

References

1 Z. Wu, B. Li, M. Chen, Y. Yang, R. Zheng, L. Yuan, Z. Li, X. Tan and H. Xu, *J. Alloys Compd.*, 2022, **901**, 163665.

2 X. Yan, H. Guo, W. Yang, S. Pang, Q. Wang, Y. Liu, P. K. Liaw and T. Zhang, *J. Alloys Compd.*, 2021, **860**, 158436.

3 H. Zhang, W. Li, H. Xu, L. Chen, J. Zeng, Z. Ding, W. Guo and B. Liu, *Coatings*, 2022, **12**, 628.

4 C. H. Lin and J. G. Duh, *Surf. Coat. Technol.*, 2008, **203**, 558-561.

5 H. Zhou, L. Jiang, L. Jia, S. Zhu, L. Wang, A. Wu and X. Zhang, *J. Alloys Compd.*, 2023, **959**, 170579.

6 H. Liu, L. Jiang, J. Hu, J. Jin, X. Zhang and J. Ding, *Chem. Eng. J.*, 2024, **499**, 156267.

7 A. Savan, T. Allermann, X. Wang, D. Grochla, L. Banko, Y. Kalchev, A. Kostka, J. Pfetzing-Micklich and A. Ludwig, *Materials*, 2020, **13**, 2113.

8 V. Maier-Kiener, B. Schuh, E. P. George, H. Clemens and A. Hohenwarter, *Mater. Design*, 2017, **115**, 479-485.

9 Y. Hong, C. Zhou, Y. Zheng, L. Zhang and J. Zheng, *Mat. Sci. Eng. A-Struct.*, 2021, **799**, 140279.

10 M. J. Uddin, E. Ramirez-Cedillo, R. A. Mirshams and H. R. Siller, *Mater. Charact.*, 2021, **174**, 111047.

11 F. K. Yan, B. B. Zhang, H. T. Wang, N. R. Tao and K. Lu, *Scr. Mater.*, 2016, **112**, 19-22.

12 J. Hu, L. Jiang, H. Liu, J. Jin, L. Jia, A. Wu and X. Zhang, *J. Mater. Chem. C*, 2024, **12**, 16015-16024.

13 J. Yang, L. Jiang, Z. Liu, Z. Tang and A. Wu, *J. Mater. Sci. Technol.*, 2022, **113**, 61-70.

14 L. Jia, L. Jiang, J. Hu, J. Jin, S. Yan, A. Wu and X. Zhang, *Acs Appl. Mater. Inter.*, 2023, **15**, 58651-58662.

15 Q. Ban, Y. Li, L. Li, Y. Qin, Y. Zheng, H. Liu and J. Kong, *Carbon*, 2023, **201**, 1011-1024.

16 H. Pang, Y. Duan, M. Gao, L. Huang, X. Liu and Z. Li, *Mater. Today Nano*, 2022, **20**, 100243.

17 J. Hu, L. Jiang, L. Jia, J. Jin, A. Wu and X. Zhang, *Carbon*, 2024, **228**, 119406.